ELSEVIER

NDT&E International 35 (2002) 165–175

NDT&E international

www.elsevier.com/locate/ndteint

# Neural network based defect detection and depth estimation in TNDE

Akbar Darabi, Xavier Maldague*

*Electrical and Computing Engineering Department, Université Laval, Quebec City, Que., Canada G1K 7P4*

Received 15 September 2000; revised 19 May 2001; accepted 13 June 2001

**Abstract**

For many years, applications of the TNDE (Thermographic NonDestructive Evaluation) technique has been limited due to the complex non-linearity nature of related inversion problems such as defect depth estimation. Artificial neural networks have recently obtained success in revealing and providing quantitative information concerning defects in TNDE. In this paper, a three dimensional thermal model for non-homogenous materials such as carbon fiber reinforced plastic (CFRP) is first given. The modeling results are compared with the analytical solution based on Duhamel's theorem. Two back propagation neural networks (NN) as defect detector and depth estimator are then presented. Finally, simulated and experimental results are presented and discussed. 

*Keywords*: Neural networks; Defect detection; Depth estimation; Infrared thermography

## 1. Introduction

For several years, infrared measurement and inspection techniques have been used to inspect and evaluate subsurface defects, thermo-physical properties, coating thickness and hidden structures. Based on thermal wave propagation and attenuation analysis, each thermal non-homogeneity perturbs the propagation of the thermal waves and changes the temperature response on the specimen surface as compared to the surrounding sound region. The thermal perturbation is recorded by an infrared detector to provide information for further processing [1–3]. Advantages of non-invasiveness, safety and relatively low cost are among the appreciated advantages of this approach, while on the other hand, presence of noise, limited resolution and probing depths are the most disturbing aspects. In active (Thermographic NonDestructive Evaluation) TNDE, thermal stimulation can be done mainly by a pulse (Pulsed Thermography, 'PT') or sinusoidal (Modulated Thermography, 'MT') heating source. In the PT approach, the sample under investigation is heated for a time period varying from ms to s. The duration of the heating pulse depends on thickness and thermo-physical properties of the sample. Usually, the analysis of the transient temperature is done in the time domain. Recently, a frequency analysis of PT based on the Fourier transform has been employed to detect and characterize subsurface defects. This approach is called PPT (Pulsed Phase Thermography) with advantages of both PT and MT approaches [4].

In recent years many researchers have used neural networks to solve complex non-linear real world problems. Neural networks (NN) are potentially powerful, robust and adaptive tools for detecting and classifying targets under changing signature or environmental conditions. They can learn from a provided training set and generalize these examples to other data which are not contained in the training set [5,6].

Artificial neural networks (ANN) as a TNDE defect detector and classifier have been proposed in the past few years [7–12]. Multilayer perceptrons were employed to detect and characterize defects using phase data extracted from the PPT method [7,9]. These studies revealed that phase data has limited sensitivity to noise and requires sufficiently high sampling rate with respect to thermal properties of specimens to achieve its complete potential. A comparison of Kohonen and perceptron NNs performances applied to TNDE was made in [8]. This study showed that perceptron NN achieves much better detection results. In [10], two multi-layer neural networks were used to reveal and estimate corrosion severity in aluminum. The network inputs are temperature vs time curves and their outputs show defect or non-defect status and corresponding estimated depth for processed pixels. The other attempt involves the use of experimental and simulated data combined together to train multi-layer networks with input vectors containing only the maximum contrast and its occurrence time for each

* Corresponding author. Tel.: +1-418-656-2962; fax: +1-418-656-3594.
*E-mail addresses:* darab@gel.ulaval.ca (A. Darabi), maldagx@gel.ulaval.ca (X. Maldague).

0963-8695/02/$ - see front matter 
PII: S0963-8695(01)00041-X

pixel, while the output indicates estimated depth and defect or non-defect alarm for each pixel [11,12].

This paper will investigate the development and use of various NN architectures for defect feature extraction and detection for non-homogeneous material such as carbon fiber reinforced plastic (CFRP) in TNDE. We intend to use only simulated data during the training phase. This allows to train NNs with non-redundant and representative data on one hand and study noise effects on NN performances on the other hand.

## 2. Transient heat transfer modeling

When a temperature gradient exists in a body, experience shows there is an energy transfer from the high-temperature region to the low-temperature region. This energy is transferred by conduction. For a medium with constant thermal conductivity $k$ (i.e. independent of position and temperature), as well as approximately constant specific heat $C_p$, density $\rho$ and no internal heat generation, the heat conduction equation can be formulated as [13]:

$$\nabla^2 T(\mathbf{r},t) = \frac{1}{\alpha}\frac{\partial T(\mathbf{r},t)}{\partial t} \tag{1}$$

where $T(\mathbf{r},t)$ is the time-dependent temperature ($\mathbf{r}$ is a spatial vector and $t$ is the time variable) and $\alpha = k/\rho C_p$ is the thermal diffusivity of the medium with units in $m^2\,s^{-1}$. Eq. (1) is called the diffusion or Fourier equation [13]. It follows that the heat conduction equation for an isotropic body in absence of volumic power density and expressed in a rectangular coordinate system $(x, y, z)$ is [13,14]:

$$\frac{\partial}{\partial x}\left(k_x\frac{\partial T}{\partial x}\right) + \frac{\partial}{\partial y}\left(k_y\frac{\partial T}{\partial y}\right) + \frac{\partial}{\partial z}\left(k_z\frac{\partial T}{\partial z}\right) = \rho C_p\frac{\partial T}{\partial t} \tag{2}$$

The differential Eq. (2) has numerous possible solutions. To obtain a particular solution, the differential equation of heat conduction requires specifying both boundary conditions and initial conditions (for time-dependent problem). The initial condition sets the initial ($t_s = 0$) temperature distribution and the boundary conditions of the medium set the temperature or the heat flow at the boundaries of the region (e.g. a known temperature, an insulated boundary or heat dissipation by convection or radiation from the boundary surface).

Obtaining an analytical solution from Eq. (2) is extremely difficult, except for a few simple geometries. Numerical computation techniques, based on discretization of space and time, such as the finite difference or finite element methods are often preferred for most practical problems. In this study we use a finite-difference method in which the initial statement of the problem in differential form (based on Eq. (2)) is changed to a finite difference statement by substituting difference relations for partial temperature derivatives of time and space. The idea is to represent the workpiece by a mesh of elementary volumes of material. A node is associated with each volume and is representative of the corresponding thermal behavior of the volume it is associated with. Next, temperature differences between adjacent nodes are computed at each time step (e.g. details can be found in Ref. [1], Section 3.4.2). This thermal modelling applied to TNDE was implemented on a MasPar MP-1 (Massively Parallel) computer [14].

## 3. Delamination model description

Delamination defects are characterized by air gaps between two plies in composite laminate materials such as CFRP. These structural discontinuities produce an interface thermal resistance that causes heat flux perturbation during the transient thermographic procedure.

The specimen studied is shown schematically in Fig. 1. It is a CFRP block, which contains an air gap as simulated defect. It is assumed that the sample surface is uniformly heated by a heating source (such as flash lamps, laser or electrical heaters) for a time $t$. Here, we specify a finite-size delaminated defect involved into the solution of 3D heat conduction equation (Eq. (2)) with boundary and initial conditions such as expressed as follow (more details can be found in p. 39, Ref. [14]):

$$0 \le x \le L_1; 0 \le y \le L_2; 0 \le z \le L_3$$

$$T_{(x,y,z,\tau=0)} = 0$$

$$\frac{\partial T_{(x,y,z=0)}}{\partial z} = -\frac{q}{k_z} + \frac{h_c}{k_z}T_{(x,y,z=0)} + \frac{h_r}{k_z}((T_{(x,y,z=0)} + 273)^4 - 273^4)$$

$$\frac{\partial T_{(x=0,y,z)}}{\partial x} = 0$$

$$\frac{\partial T_{(x,y=0,z)}}{\partial y} = 0$$

$$\frac{\partial T_{(x=L_1,y,z)}}{\partial x} = 0$$

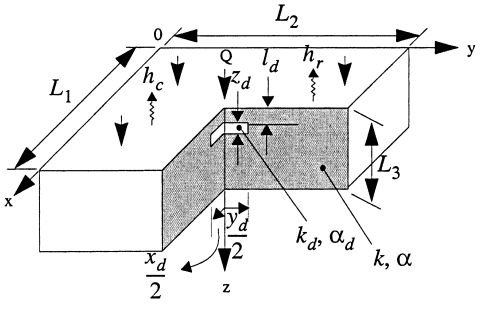


Fig. 1. Schematic diagram of the modeled CFRP sample.

$$\frac{\partial T_{(x,y=L_2,z)}}{\partial y} = 0$$

$$\frac{\partial T_{(x,y,z=L_3)}}{\partial z} = 0$$

The initial temperature here is set to 0°C (273 K), $q$ is the input heat flux, $h_c$ and $h_r$ are respectively the convection and radiation heat exchange coefficients. In order to study the behavior of defect signals, we consider a sample, which contains an air gap. The dimensions of the CFRP block are $L_1 = 96$ mm, $L_2 = 96$ mm and $L_3 = 2$ mm. The defect is a $1.5 \times 1.5$ cm square with thickness of 100 mm at depth 700 mm. The thermal properties and heating–cooling parameters are as follows:

- thermal properties [1]:
  for CFRP

  $\alpha_x = \alpha_y = 3.7 \times 10^{-6}\ \mathrm{m^2\ s^{-1}}$

  $\alpha_z = 0.42 \times 10^{-6}\ \mathrm{m^2\ s^{-1}}$

  $k_x = k_y = 7\ \mathrm{W\ m^{-1}\ °C^{-1}}$ (parallel to the fibers)

  $k_z = 0.8\ \mathrm{W\ m^{-1}\ °C^{-1}}$ (perpendicular to the fibers)

  for air defect

  $\alpha = 33 \times 10^{-6}\ \mathrm{m^2\ s^{-1}}$

  $\mathrm{k} = 0.024\ \mathrm{W\ m^{-1}\ °C^{-1}}$

- heating–cooling parameters:

  $q = 100\ \mathrm{kW\ m^{-2}},\ h_c = 10\ \mathrm{W\ m^{-2}},\ h_r = 5.67 \times 10^{-8}\ \mathrm{W\ m^{-2}}.$

The simulated temperature profiles over defect (o-dotted curve) and sound (·-dotted curve) areas on the sample surface are shown in Fig. 2(a). As seen, the thermal perturbation due to the defect is distinguishable. In the following sections, we will explain how it is possible to enhance the thermal contrast between these two curves and use it to reveal and estimate defect parameters. An example of such an enhancement is the defect–sound difference shown in Fig. 2(b).

## 4. The analytical solution of the heat conduction problem applied to TNDE

The following step is to consider the pulse-transient IR thermography, in which the sample is heated by a heat pulse source and then a time sequence of images is recorded to give the temperature decay on the surface of the inspected sample [1–3]. In sound area far from defects, we can suppose that the sample behaves as an adiabatic plate heated by a square pulse [15]. This simple configuration is shown in Fig. 3.

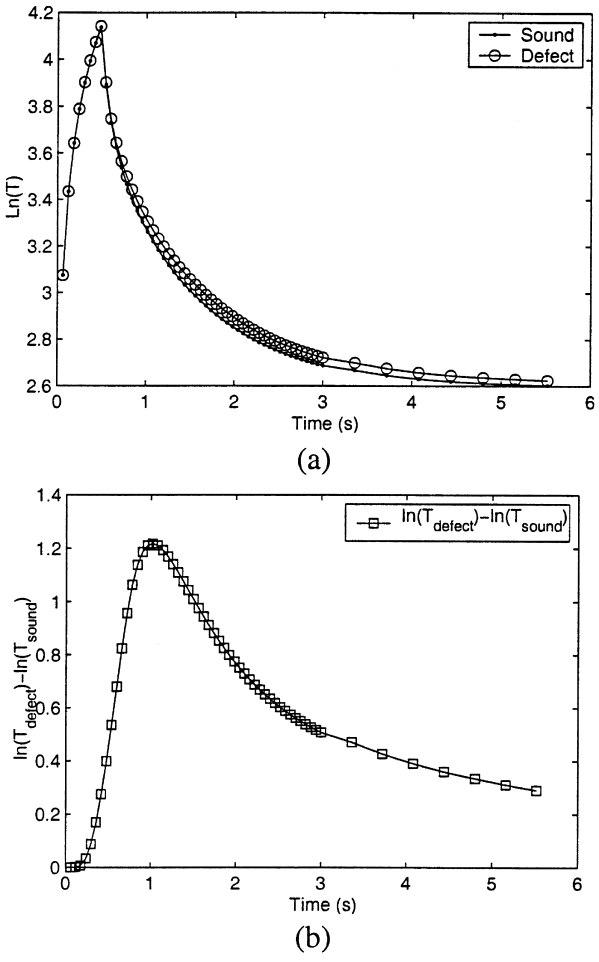


Fig. 2. The computed temperature evolution over: (a) defect and sound areas (b) their difference on the CFRP sample surface.

The plate with thickness $L$ is initially at zero temperature differential with respect to ambient temperature. For times $t > 0$ the boundary surface at $z = L$ is kept insulated while the surface at $z = 0$ is subjected to a heat pulse flux as:

$$-k\frac{\partial T}{\partial z} = f(t) = \begin{cases} Q & for \quad 0 < t < \tau_h \\ 0 & for \quad t < \tau_h \end{cases} \tag{3}$$

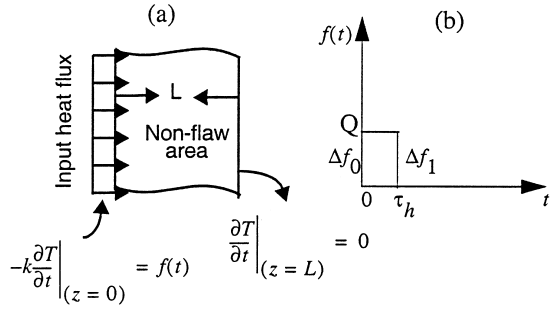


Fig. 3. (a) Model heating (b) shape of the heating pulse.

The analytic solution of the Eq. (1) using Duhamel's theorem with the considered boundary conditions on the surface, $f(t)$, and given initial conditions, the temperature at the sample surface sample is obtained with [16]:

$$T(0,t) = \frac{QL}{k_z}\left(Fo + \frac{2}{\pi^2}\sum_{m=1}^{\infty}\frac{1}{m^2}(1 - e^{-m^2\pi^2 Fo})\right) \quad (4)$$

for $0 < t < \tau_h$

$$T(0,t) = \frac{QL}{k_z}\left(Fo_h + \frac{2}{\pi^2}\sum_{m=1}^{\infty}\frac{1}{m^2}(e^{-m^2\pi^2(Fo-Fo_h)} - e^{-m^2\pi^2 Fo})\right)$$

for $t > \tau_h$ (5)

where $Fo = \alpha\tau/L^2$ is the Fourier number and $Fo_h = \alpha\tau_h/L^2$ is the Fourier number of time of maximum excess temperature. Fig. 4 shows the temperature curves obtained from numerical (Eq. (2)) and analytical solution (Eqs. (4) and (5)) for a CFRP sample (containing no defects) with thickness $L = 2$ mm, thermal properties $\alpha_z = 0.42 \times 10^{-6}$ m$^2$ s$^{-1}$, $k_z = 0.8$ W m$^{-1}$ °C$^{-1}$ and a heat pulse with $Q = 100$ kW m$^{-1}$ and $\tau_h = 0.5$ s as shown in Fig. 3(b).

In Fig. 4, the '···'dotted curve corresponds to the numerical solution and the 'ooo' dotted curve corresponds to the analytic solution of the 1D heat conduction problem. These two curves match well (maximum discrepancy is less than 1.6°C after the heating pulse), therefore the numerical solution can be considered sufficiently accurate to be used for TNDE applications.

## 5. Thermal data

The numerical modelling of Section 4 is now used to produce the necessary synthetic thermal data for different subsurface defect geometries in the samples. Let us consider a CFRP sample block with dimension of $9.6 \times 9.6 \times 2$ mm (Fig. 5). This sample contains five air delaminations of

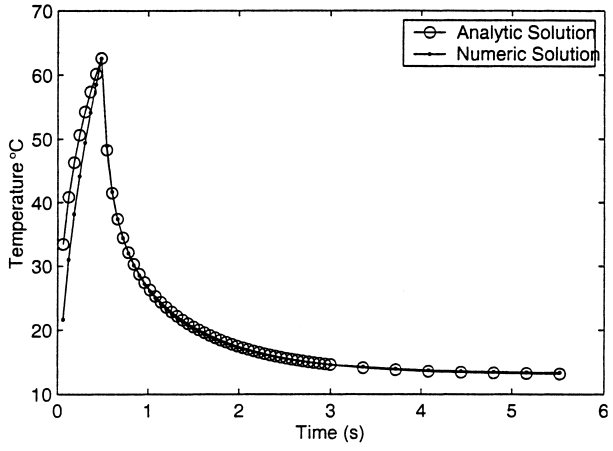


Fig. 4. Surface temperature evolution of CFRP block computed using both analytical and numerical solution methods.

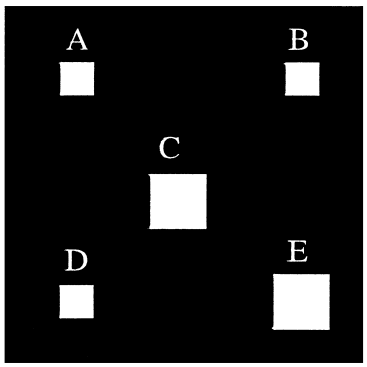


Fig. 5. A CFRP block sample, which contains five air delamination defects A, B, C, D, and E of thickness 100 mm at depths respectively 0.6, 1.4, 1.0, 0.2 and 0.7 mm.

different sizes positioned at depths 0.6, 1.4, 1.0, 0.2 and 0.7 mm.

As seen in Fig. 2, classifying sound and defect areas in two different classes is not evident in most cases, if we consider temperature evolution on the sample surface as input data to the neural network. To enhance data difference between sound and defect areas, we can use the thermal contrast curve as input [11]. There are four informative parameters: $\Delta T$-image, thermal contrast, running-contrast and normalized contrast which are mostly employed in transient TNDE [1,15]. The running contrast, which will be used as input data to the detector and depth estimator neural networks, is defined as follows [3,15]:

$$C^r(t) = \frac{T_{\text{defect}}(t) - T_{\text{sound}}(t)}{T_{\text{sound}}(t)} \quad (6)$$

where $T_{\text{sound}}(t)$ and $T_{\text{defect}}(t)$ are respectively sound and defect area temperatures and $t$ is the time variable. Fig. 6 shows running-contrast curves for the sample of Fig. 5. The curve with dash-doted line is the contrast curve over the randomly

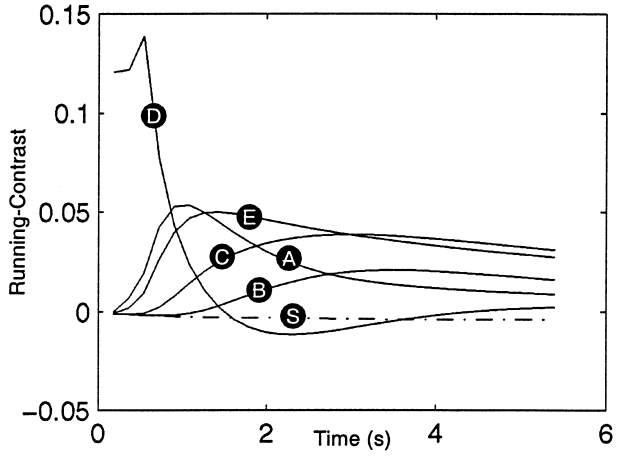


Fig. 6. The running temperature contrast vs time curves for one randomly chosen sound pixel (dash-doted line) and central pixels of five air defects A, B, C, D and E (solid lines) which are respectively located in the CFRP block at depth 0.6, 1.4, 1.0, 0.2 and 0.7 mm.

chosen sound pixel and curves with solid lines are related to the central pixels of the defects. Comparison of these contrast curves to the absolute temperature curves, depicted in Fig. 2(a) indicates that the running-contrast curves can be classified as defect or non-defect, depending on their pixel thermal properties. After having classified pixels into defect and non-defect classes, the pixels corresponding to defects can then be classified into different classes with respect to their depths.

## 6. Defect detector network

Neural networks can be considered as parallel processors. They are composed of a large number of highly interconnected processing elements (neurons) working together to solve specific problems [17]. In this study, we are only interested in multi-layer perceptron networks (MLP), which are supervised networks. The MLP network is a nonparametric technique for performing a wide variety of detection and estimation tasks. The MLP network can be trained using the back propagation algorithm, which is probably the most used learning algorithm in the recent years. This algorithm has been applied to a wide variety of real problems [17].

The most important problem that must be solved when a back-propagation NN is used consist in determining the number of neurons in each layer, the connections and their weights. In feedforward networks (MLP), connection weights are initialized to random values and then adjusted during the training procedure to satisfy a specific error goal. In this study, we have examined many different feedforward network architectures as defect detector. This analysis indicated that there is a correlation between the maximum defect depth at which the contrast over a defect area is different from the contrast over a sound area and the optimum number of units in the hidden layers.

After different tests, we settled for a $30 \times 15 \times 1$ defect detector network whose architecture is shown in Fig. 7. This network was trained using 130 input–output pair vectors extracted from the samples which contained air delamination defects at different depths and configurations, 105 input vectors were running-contrast curves over defect areas and 25 were over sound area. Fig. 8 shows the maximal points of

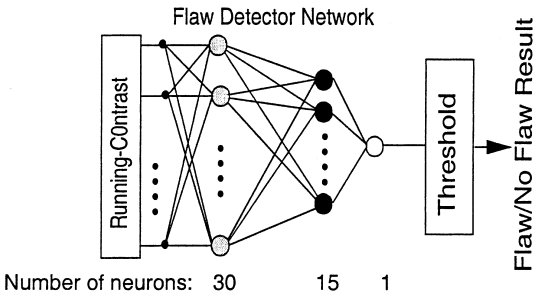


Fig. 7. A three layer defect detector network architecture.

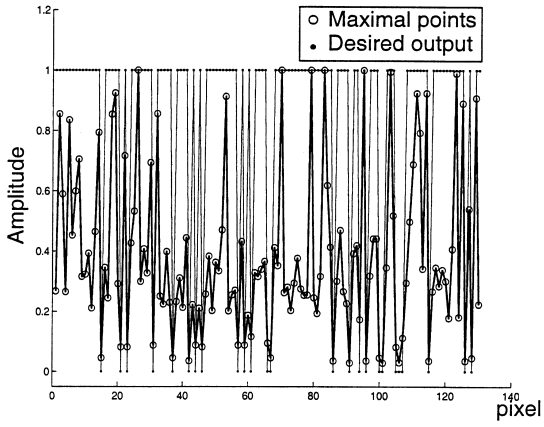


Fig. 8. The maximal points of thermal contrast curves and corresponding desired outputs.

input curves and desired output which is '0' for non-defect pixel and '1' for defect pixel.

### 6.1. Simulation results for detector network

The trained network was provided with nine other simulated samples containing five air delamination defects with the same shape (Fig. 5) of defects which were used during the training procedure. As shown in Table 1, the deepest defect is located at depth 1.4 mm and the shallowest defect is located at depth 0.1 mm. The network output results for these test samples are shown in Figs. 9 and 10. Fig. 9 shows that the detector network detected all the defects in these nine simulated samples. The white and black pixels in this figure define respectively, defect and sound areas. Fig. 10 shows the error pixels (white pixels) which are 3.2% of the total pixels. This means the network correctly classified 96.8% of the total pixels (as being either *defect* or *non-defect pixels*).

The second experiment involved the use of additive noisy data to examine the proposed network performance. The task was similar to the one above but noisy data was generated based on white Gaussian noise with different temperature noise standard deviations $\sigma_T$(°C) as input test

Table 1
The simulated samples depth profile which were deployed to examine defect detector network performance

| Sample | Defect/depth (mm) | | | | |
|---|---|---|---|---|---|
| | A | B | C | D | E |
| #1 | 0.9 | 1.1 | 0.5 | 0.8 | 0.3 |
| #2 | 1.3 | 0.9 | 0.3 | 0.2 | 0.7 |
| #3 | 0.6 | 1.4 | 1.0 | 0.7 | 0.2 |
| #4 | 0.4 | 1.3 | 0.2 | 1.0 | 0.1 |
| #5 | 0.9 | 0.2 | 1.4 | 1.1 | 0.5 |
| #6 | 1.1 | 0.8 | 0.4 | 1.2 | 0.1 |
| #7 | 0.1 | 0.4 | 1.2 | 0.5 | 1.4 |
| #8 | 1.2 | 0.6 | 1.1 | 0.3 | 0.8 |
| #9 | 0.7 | 0.3 | 0.6 | 1.3 | 1.0 |

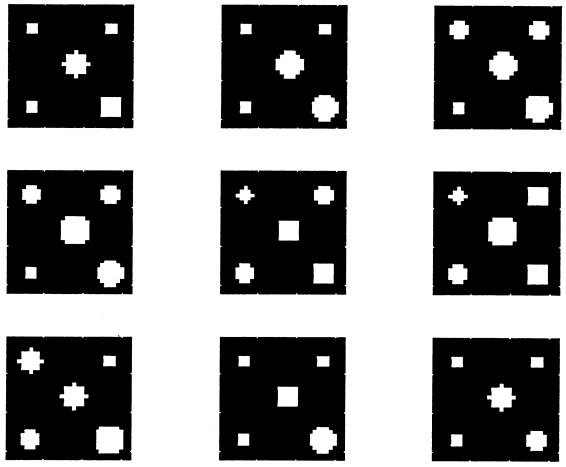

Fig. 9. Defect detector output images for nine different simulated data sets, white pixels represent defect areas.

signals. The temperature noise standard deviations at different temperatures for the available Cincinnati Electronics IRC-160 infrared camera are given in [18]. The Cincinnati Electronics IRC-160 noise standard deviation decreases when the specimen temperature increases. Also, we know that in active thermography the sample is heated for a short period of time by the heating source. Consequently, the sample surface temperature will be above the ambient temperature (about 25.0°C) for most of our applications. Therefore, we supposed the Cincinnati Electronics IRC-160 noise standard deviation in the worse case for our applications as $\sigma_T(°C) = 0.039$ [18].

The previous experimental data sets were thus contaminated with white Gaussian noise with noise standard deviation $\sigma_T(°C) = 0.054$ and also, in a second trial with $\sigma_T(°C) = 0.039$. The detector network output results for these additive noisy input data sets are presented in Fig. 11(a) and (b), respectively. In this experiment, for both cases, the defect detector is able to reveal all defects contained in the sample. However the network output results are degraded by the presence of white Gaussian noise in the input data sets. For contaminated input data sets with noise of $\sigma_T(°C) = 0.054$, the overall output results error is 11.2% and with the noise with $\sigma_T(°C) = 0.039$, it is 6.3%.

The defects in all tests so far were well separated and for each defect, all pixels were laid at the same depth with regular defect shapes. Therefore in these previously analyzed cases temperature perturbations due to the defects were symmetrical both in defect areas and around them. We now consider a sample which contains a T-shaped air defect (Fig. 12(a)) and in which the pixels depth gradually changes (Fig. 12(b)). This type of defect requires a three-dimensional heat transfer modeling such as the 3D thermal simulation described previously.

In this case, the network correctly classified about 95% of the image pixels and the T-shaped defect is well resolved, as shown in Fig. 13(a). The network error image is shown in Fig. 13(b). This confirms that the lateral defect effect is more significant in shallow defect areas (see arrows).

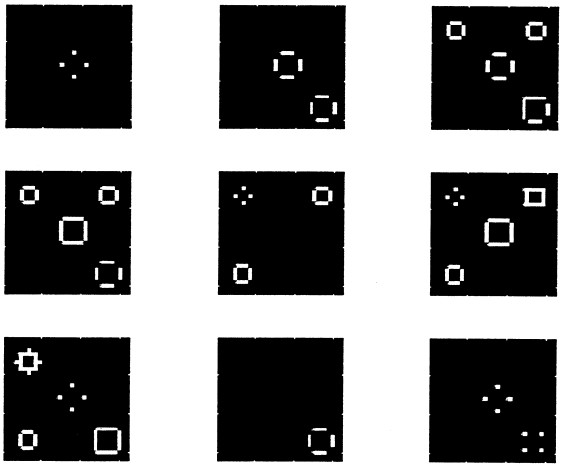

Fig. 10. Error images for the defect detector of Fig. 9. White pixels shows pixels incorrectly detected as defect or non-defect pixels.

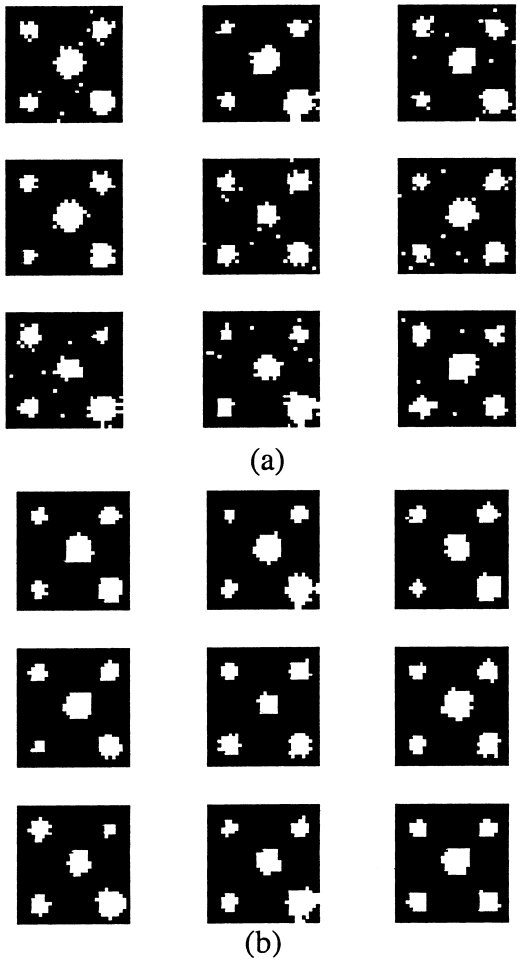


Fig. 11. Defect detector output images for the simulated data sets which are contaminated with a white Gaussian noise (a) $s = 0.054$ and (b) $s = 0.039$.

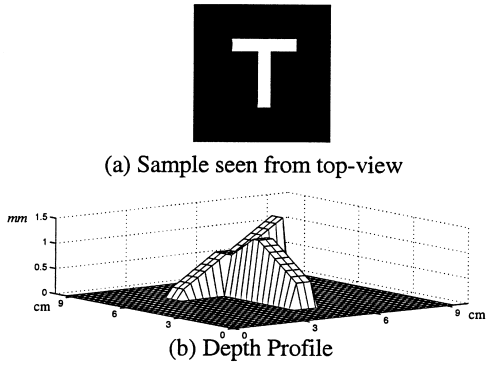


Fig. 12. A CFRP sample containing a T-shape air defect with shown depth profile. (a) Sample seen from top-view (b) depth profile.

### 6.2. Experimental results for detector network

The network classification ability is now evaluated in this section using real thermal data sets. Since we had at our disposal CFRP samples containing Teflon™ delamination defects, we had to provide simulated samples containing Teflon™ delamination defects in order to train the detector network (Fig. 14).

The simulated thermal data for CFRP samples submitted to a heat source with a power of about 100 kW $m^{-2}$ for a 0.5 s period of time, shows that the contrast signal is the same as for a sound pixel, if the Teflon™ defect is located deeper than 1.1 mm, such as defect B in Fig. 15 (we intentionally added 0.005 as offset to this contrast signal just to distinguish it from the sound pixel contrast signal (the dash-doted curve). Moreover, the temperature contrast amplitude for each defect pixel depends on the pixel distance from the defect center due to the lateral thermal diffusion [19]. The maximum contrast occurs at the central pixel while the minimum contrast belongs to the farthest pixel from the defect center. For example, Fig. 16 shows contrast curves of all 12 pixels in defect E region. Although the amplitude of these contrast signals varies over the pixels of this defect located at a fixed depth from sample surface, the time of the maximum amplitude is roughly the same for all of them. Therefore, it is sufficient to define four representative pixels among these 12 pixels to correctly represent defect E to the network during the training procedure.

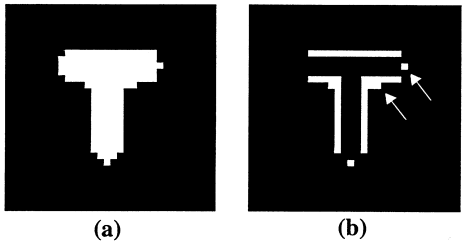


Fig. 13. Detector network output result (for specimen of Fig. 12): (a) White area detected as defect, (b) The error pixels (white) which are incorrectly classified as defect or sound pixels.

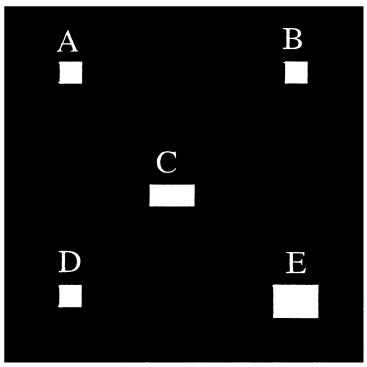


Fig. 14. Simulated CFRP sample containing Teflon™ defects which are used in the training procedure for experimental results.

Considering the above mentioned criteria, the defect detection network was trained with 136 normalized contrast vectors chosen from both sound and defective areas. After training, two CFRP samples were used in the testing phase. The first sample contains various inserted rectangular Teflon™ defects with thickness of 50 μm at different depths. Many experiments were conducted to record the temperature evolution profiles for different areas of this CFRP sample. In these experiments, the sample is first heated by two flash lamps with a total power of 80 kW and then the surface temperature profiles are recorded for 5 s. Unfortunately, this procedure did not reveal all of the known buried defects. This is mainly due to the highly anisotropic nature of CFRP (making the heat propagation *easier*, laterally on the surface than transversely under the surface), non-uniform heating, flash heating (the heating period is too short to penetrate deep within the specimen), noise and other errors in the experimental procedure.

Nevertheless, useful data was obtained from these experiments. For defect areas #1 (depth = 0.15 mm) and #2 (depth = 0.46 mm), the recorded infrared data was filtered

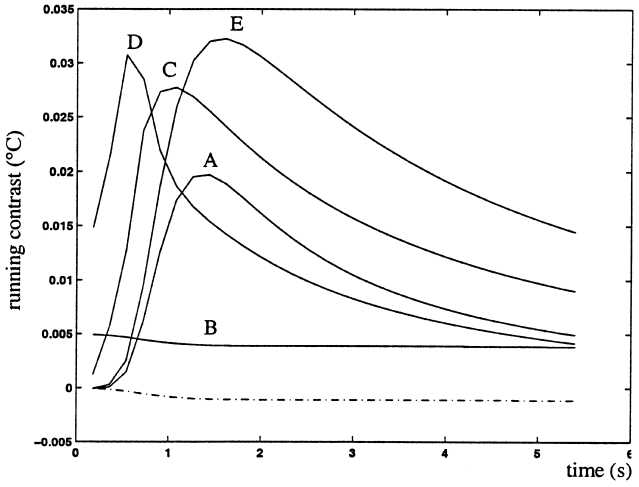


Fig. 15. The running-contrast signal over Teflon™ defects A, B, C, D, E and sound area (dash-doted curve) for the CFRP sample shown in Fig. 14. The defects depth are respectively 0.9, 1.2, 0.5, 0.3, and 0.8 mm.

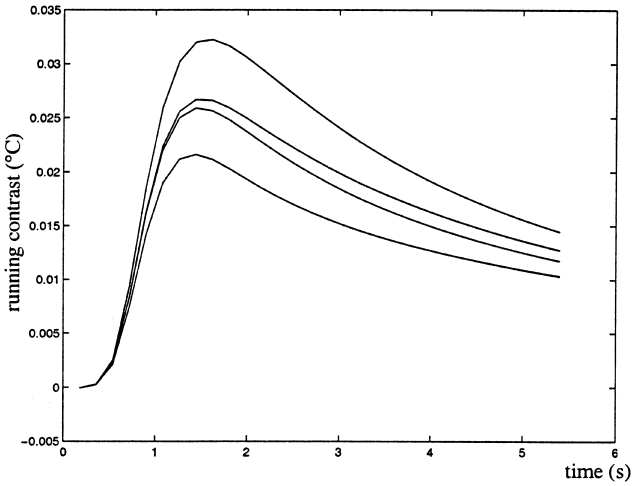


Fig. 16. The running-contrast signal curves for all pixels of defect E. This shows they can be classified in four categories.

both in time and in spacial domains. Next, the running-contrast vector was given as input to the network. The maximum contrast image and detector network output result for this experiment are shown in Fig. 17. In the maximum contrast image (Fig. 17(a)), we can observe only defect #2 with ambiguity on its border and also noise all over the image. It seems that most of this noise is due to the non-homogenous thermal properties of this CFRP sample that can not be reduced or completely removed by conventional data processing methods. The detector network result for these contrast input vectors is given in Fig. 17(b). As seen in this figure, the network is able to reveal both defects #1 and #2. Further erosion and dilatation processing could help cleaning up the resulting image. This is however not the goal of the present work [20].

The second test was done on another CFRP sample which contains two circular Teflon™ defects with 10 mm diameter at depths of 2 and 3 mm, respectively. In this experience, the sample was also heated by the flash heating source and the surface temperature was recorded for 5 s. The maximum contrast image is shown in Fig. 18(a). In this image one can roughly detect one of the defects while non-uniform heating is evident all over the sample. Now if we take the average contrast signal as reference contrast signal, then the detector network output obtained is the image represented in Fig. 18(b). Although, false alarm pixels are present in the output image, both defects are well detected (in fact these artificial embedded defects are of known shapes and locations). Moreover, in this case, if we choose another pixel as sound pixel we obtain a different result such as shown in Fig. 18(c) in which just one of the two defects is revealed but with false alarm pixels significantly reduced.

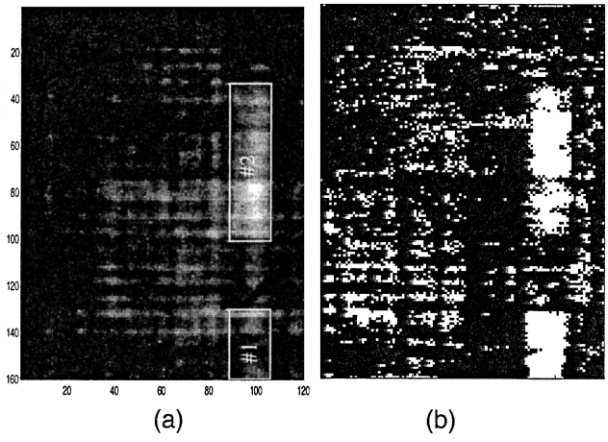


Fig. 17. The detector network output results and maximum contrast images over defects #1 and #2. (a) Maximum contrast image. (b) The network output image.

## 7. Defect depth estimation network

Extraction of subsurface defect properties such as depth, thermal resistivity and size is called inverse problem in TNDE. Many research works have been conducted to solve the inverse problem in TNDE in recent years. Analytical

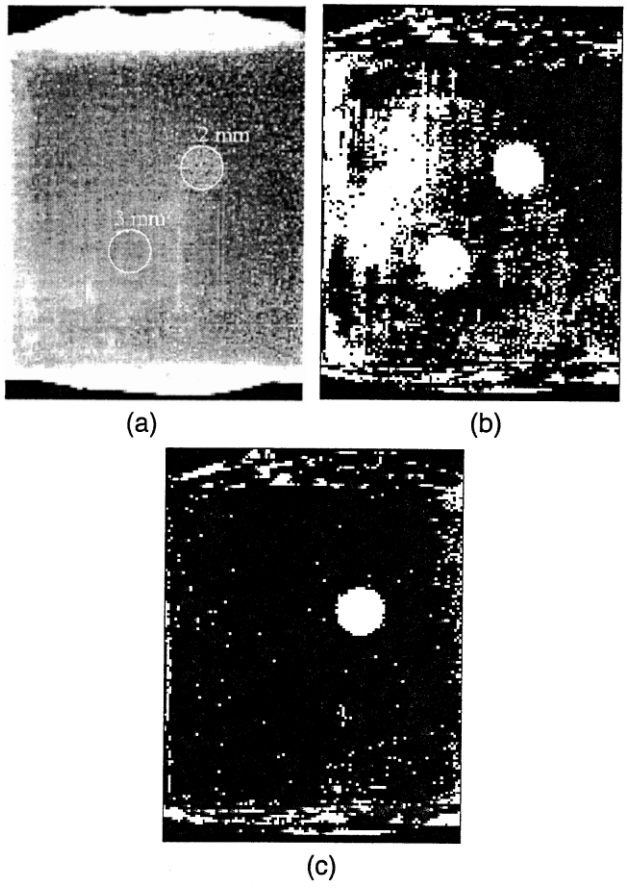


Fig. 18. The detector network output results and maximum contrast images for the CFRP sample containing two circular Teflon™ defects with 10 mm diameter at depth 2 and 3 mm. (a) Maximum contrast image. (b) The network output image supposing average contrast as reference contrast. (c) The network output image supposing one of the upper-left pixels as sound pixel.

solutions for some simple geometries can be derived by using Green Functions but for most practical cases such a solution becomes more complex or impossible [2,21].

As said before, artificial neural networks (ANN) are modern alternative to classical data analysis methods and they are employed to solve real complex problems in many applications. In this section, a depth estimator network is trained on modeled mathematical data generated to simulate an experiment such as the specimen of Fig. 5. The simulated CFRP samples contain air gaps with 100 μm thickness as defects at different depths. The simulated data study shows that an air gap defect can produce considerable contrast signal on the sample surface, if we restrict ourselves to stimulated conditions proposed in previous sections (that is to detect defects up to depth 1.5 mm). The estimator network with 20 input, 15 hidden and 15 output neurons was provided with about 140 input/output vectors as training set. The input vectors for the depth estimator network are contrast vectors as for the defect detector network but now the output vectors are defined as pixel depth. If the pixel belongs to the sound area the output vector value will be zero. Otherwise if it is a defect pixel with specific depth, then the output vector value should correspond to the defect pixel depth (expressed in mm).

### 7.1. Simulation results for estimator network

The estimator network performance is also tested by both simulated and experimental data. The first data set is obtained from the same sample, which was used during the training procedure. The contained defects are located at depth 1.1, 0.9, 0.5, 0.8, and 0.3 mm. The original and estimated depth profiles pixel by pixel are shown in Fig. 19. Fig. 19(b) shows the network response to input contrast data without additive noise while Fig. 19(c) depicts the estimated depth profile for contaminated input data with a Gaussian noise ($\sigma = 0.033$ and $\eta = 0$). Comparing these results with the original depth profiles, we find that the network can estimate all defect depths. The estimated defect depths are 1.2, 0.9, 0.5, 0.8 and 0.3 mm even if additive noise increases the error pixels and in some case modifies the estimated depth. It is noted that a criterion threshold on obtained decisions could be possibly added to limit the number of error pixels. Moreover, the known *Tanimoto criterion* is also a good tool to assess the validity of a detection procedure ([1], p. 219).

We also examined the estimator network performance with a simulated data set extracted from the sample which contains a T-shaped defect as shown in Fig. 12. The depth is gradually changed row per row or column per column as seen in Fig. 20(a). Although, such kind of defects was not present in the training set, the network was able to estimate the depth of the pixels. The network output is depicted in Fig. 20(b). This figure shows that most of error pixels have estimated depths greater than their neighbor defect pixel depth. To show the estimated depth accuracy, we show in

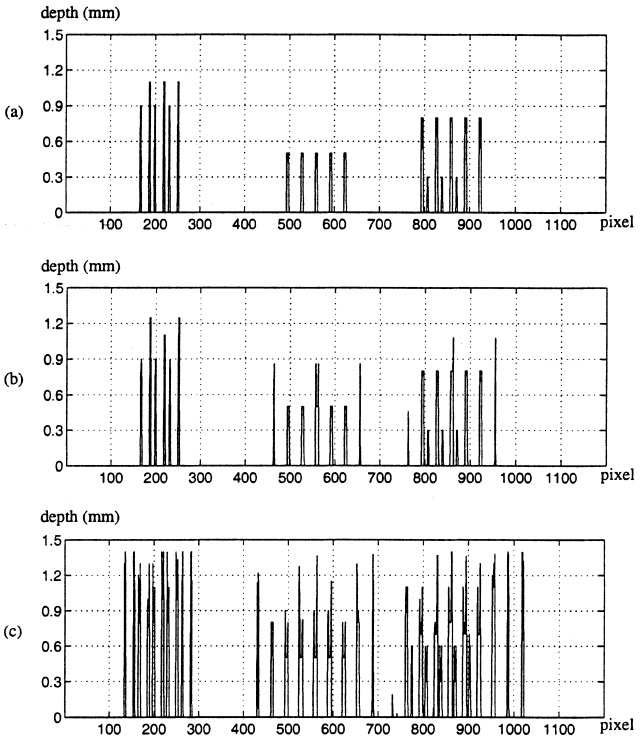


Fig. 19. The original and estimated defect depth profiles for a sample which was used during training procedure: (a) Original depth. (b) Estimated depth for input data without noise. (c) Estimated depth for contaminated input data with a Gaussian noise ($s = 0.033$ and $h = 0$).

Fig. 20(c) the depth profile after removing all of the error pixels. This figure shows that the estimated depth profile is almost correct as compared with the sample profile in Fig. 20(a).

### 7.2. Experimental results for estimator network

As mentioned in previous sections, the available CFRP specimens contain Teflon™ delamination defects such as the one shown in Fig. 17. Considering simulated results explained in the detector network section, it was said that we could detect and classify defects up to 1.1 mm under the sample surface. If the required accuracy is 100 μm, then the depth estimator should be able to classify the input vectors into 11 different classes. One of the networks that we propose as estimator network is built with 15 input, 15 hidden and 4 output neurons. This network is trained with 136 simulated contrast/depth vectors. The selected pixels are the same as those chosen for the detector network training set. After training, we provide the experimental data such as for the sample shown in Fig. 17 to the estimator network. The network is able to detect and estimate both defect presence and depth. The estimated depth is about 0.3 mm for one and 0.4 mm for the other defect as shown in Fig. 21. Referring the construction layout of the specimen, depths should be 0.15 and 0.46 mm. However, these are estimated, not measured values. This possibly explains

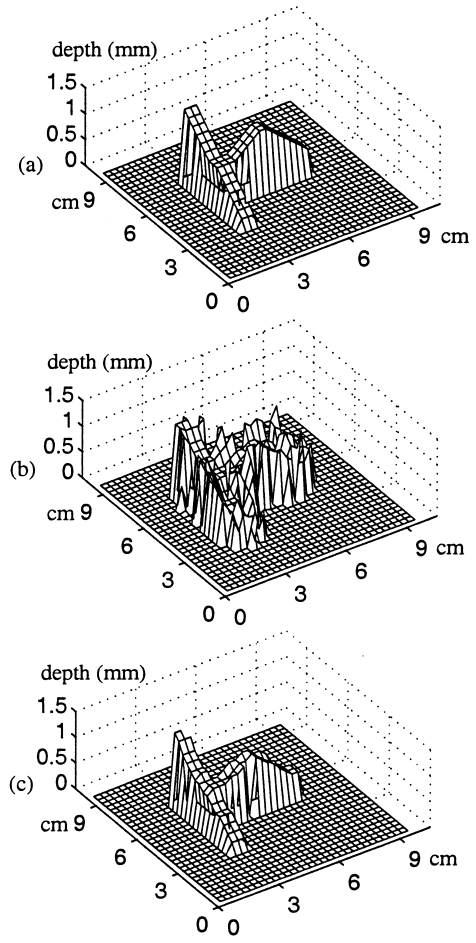


Fig. 20. Depth profiles of a CFRP sample which contains a T-shaped air defect: (a) The modelled sample depth profile. (b) Estimated depth profile. (c) The estimated depth profile with error pixels removed from the plot.

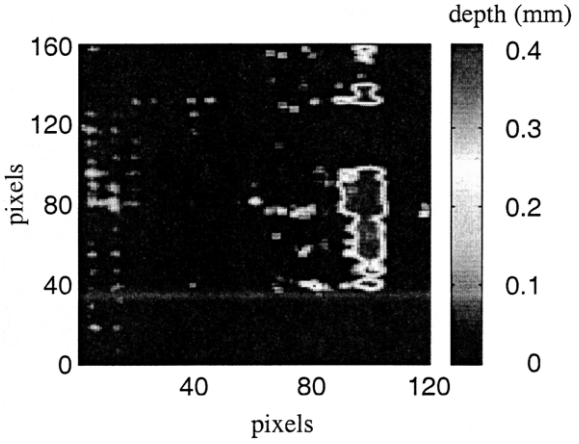


Fig. 21. Filtered output of the depth estimator neural network for a CFRP sample containing Teflon™ defect.

the noted differences (e.g. shifting of individual CFRP piled sheets — often called — *prepreg* — during curing).

## 8. Conclusions

Analysis of raw temperature and contrast data does not provide reliable classification of different regions (defect, no-defect). To enhance raw temperature differences between sound and defect regions, we used the thermal running-contrast data curves. Two multilayer backpropagation neural networks were employed for defect detection and depth estimation of specimens under investigation in TNDE. The simulated data results have shown that if the networks are properly trained they can detect and estimate defect depth even if the input data is contaminated with noise. Also, experimental results have demonstrated that NN trained by mathematical modeling data can provide a reliable means to characterize defect parameters in TNDE. To maintain a high degree of classification accuracy, the networks should be trained by representative and non-redundant data sets.

Training time for detector network, depending on the number of training set vectors, is about 2–10 min using the back propagation learning algorithm, while for the estimator network, it varies from 10 min to 2 h.

## Acknowledgements

Special acknowledgement for financial support of this research work is extended to Iranian Nation and the Ministry of Science, Research and Technology of the Islamic Republic of Iran. Support of NSERC (Canada) is acknowledged. CNR (Italy) is thanked for providing the CFRP specimen.

## References

[1] Maldague X. Theory and practice of infrared technology for non-destructive testing. New York: Wiley, 2001. 684 p.
[2] Krapez JC, Cielo P. Thermographic nondestructive evaluation: data inversion procedures, Part I: 1D analysis and experimental results. Res Nondestruct Eval 1991;3(2):81–100.
[3] Vavilov V. Thermal nondestructive testing, short history and state-of-art. QIRT 92, Eurotherm ser 27. Paris: Éditions Eurotherm, 1992. p. 179–94.
[4] Maldague X, Marinetti S. Pulse phase infrared thermography. J Appl Phys 1996;79(5):2964–8.
[5] Azimi-Sadjadi MR, Stricker SA. Detection and classification of buried dielectric anomalies using neural networks — further results. IEEE Trans Instrumn Measmt 1994;4.3(1):34–9.
[6] Miao X, Azimi-Sadjadi MR, Tian B. Detection of mine and minelike targets using principal component and neural-network methods. IEEE Trans Neural Networks 1998;9(3):454–63.
[7] Maldague X, Largouët Y, Couturier JP. A study of defect depth using neural networks in pulsed phase thermography: modeling, noise, experiments. Rev Gén Therm, vol. 37. Paris: Elsevier, 1998. p. 704–17.
[8] Vallerand S, Darabi A, Maldague X. Defect detection in pulsed

thermography: a comparison of Kohonen and perceptron neural networks. In: Wurzbach RN, Burleigh DD, editors. SPIE: thermosense XXI, vol. 3700. Bellingham, WA: SPIE Press, 1999. p. 20–5.
[9] Largouët L, Darabi A, Maldague X. Depth evaluation in pulsed phase thermography with neural network. In: Thompson DO, Chimenti DE, editors. Rev Prog Quant NDE, vol. 18A. New York: Plenum Press, 1998. p. 611–7.
[10] Prabhu DR, Winfree WP. Neural network based processing of thermal NDE data for corrosion detection. In: Thompson DO, Chimenti DE, editors. Quant NDE, vol. 12. New York: Plenum Press, 1993.
[11] Bison PG, Bressan C, Disarno R, Grinzato E, Marinetti S, Manduchi G. Thermal NDE of delamination in plastic materials by neural network processing. QIRT 94, Eurotherm Ser 42. Paris: EETI, 1995. p. 214–9.
[12] Bison PG, Marinetti S, Manduchi G, Grinzato E. Improvement of neural network performances in thermal NDE. In: Maldague X, editor. Third International Workshop — advances in signal processing for NDE of materials, vol. 3. Columbus, OH: American Soc of NDT, TONES, 1998. p. 221–7.
[13] Necati Ozisik M. Heat conduction. II. New York: Wiley, 1993.
[14] Darabi A. Massively parallel modeling of the direct problem in infrared thermography applied to the nondestructive evaluation of material, Master thesis, Université Laval, October 1995.
[15] Vavilov V, Maldague X, Dufort B, Robitaille F, Picard J. Thermal nondestructive testing of carbon epoxy composites: detailed analysis and data processing. NDT and E Int 1993;26(2):85–95.
[16] Darabi A. Detection and estimation of defect depth in infrared thermography using artificial neural networks and fuzzy Logic, PhD thesis, Université Laval, May 2000.
[17] Verma E. Fast training of multilayer perceptrons. IEEE Trans Neural Networks 1997;8(6):1314–20.
[18] Marinetti S, Maldague X, Prystay M. Calibration procedure for focal plane array cameras and noise equivalent material loss for quantitative thermographic NDT. Mater Eval 1997;55(3):407–12.
[19] Vavilov V, Maldague X, Dufort B, Robitaille F, Picard J. Thermal nondestructive testing of carbon epoxy composites: detailed analysis and data processing. NDT and E Int 1993;26(2):85–95.
[20] Dougherty ER. An introduction to morphological image processing, vol. TT9. Bellingham, WA: SPIE Press, 1992. 161 p.
[21] Krapez JC, Maldague X, Cielo P. Thermographic nondestructive evaluation: data inversion procedures Part II: 2D analysis and experimental results. Res Nondestruct Eval 1991;3:101–24.